Simulation of Neoclassical Transport with the Continuum Gyrokinetic Code COGENT

M. Dorf, R. Cohen, M. Dorr, T. Rognlien, J. Hittinger, J. Compton, P. Colella, D. Martin, P. McCorquodale

May 7, 2013

Disclaimer

This document was prepared as an account of work sponsored by an agency of the United States government. Neither the United States government nor Lawrence Livermore National Security, LLC, nor any of their employees makes any warranty, expressed or implied, or assumes any legal liability or responsibility for the accuracy, completeness, or usefulness of any information, apparatus, product, or process disclosed, or represents that its use would not infringe privately owned rights. Reference herein to any specific commercial product, process, or service by trade name, trademark, manufacturer, or otherwise does not necessarily constitute or imply its endorsement, recommendation, or favoring by the United States government or Lawrence Livermore National Security, LLC. The views and opinions of authors expressed herein do not necessarily state or reflect those of the United States government or Lawrence Livermore National Security, LLC, and shall not be used for advertising or product endorsement purposes.

Simulation of Neoclassical Transport with the Continuum Gyrokinetic Code COGENT

M. A. Dorf[1] , R. H. Cohen[1], M. Dorr[1], T. Rognlien[1], J. Hittinger[1], J. Compton[1], P. Colella[2], D. Martin[2], and P. McCorquodale[2]

[1]*Lawrence Livermore National Laboratory, Livermore, California 94550 USA*

[2]*Lawrence Berkeley National Laboratory, Berkeley, California 94720 USA*

The development of the continuum gyrokinetic code COGENT for edge plasma simulations is reported. The present version of the code models a nonlinear axisymmetric 4D ($\mathbf{R}$, $v_\parallel$, μ) gyrokinetic equation coupled to the long-wavelength limit of the gyro-Poisson equation. Here, $\mathbf{R}$ is the particle gyrocenter coordinate in the poloidal plane, and $v_\parallel$ and μ are the guiding center velocity parallel to the magnetic field and the magnetic moment, respectively. The COGENT code utilizes a fourth-order finite-volume (conservative) discretization combined with arbitrary mapped multiblock grid technology (nearly field-aligned on blocks) to handle the complexity of tokamak divertor geometry with high accuracy. Topics presented are the implementation of increasingly detailed model collision operators, and the results of neoclassical transport simulations including the effects of a strong radial electric field characteristic of a tokamak pedestal under H-mode conditions.

I. INTRODUCTION

Due to a wide range of collisionality regimes, short radial length scales for density and temperature variations (comparable to particle drift orbit excursions), and scale lengths along the magnetic field comparable to collisional mean free paths, a kinetic simulation is required for an accurate modeling of transport processes in the edge of a tokamak [1]. Presently, there are two main approaches to solving a kinetic equation: (i) the particle-in-cell (PIC) method, in which one uses macroparticles to integrate along the characteristic of the kinetic equation [2-5], and (ii) the continuum method in which the kinetic equation is discretized on a phase-space grid [6-8]. The application of the PIC approach to some important problems of tokamak edge dynamics may, however, require a very large number of macroparticles to suppress numerical noise. Among

these problems is the simulation of low-amplitude turbulence under H-mode conditions, subject to an adequate representation of the background quasi-equilibrium dynamics [1]. Moreover, even for the case of axisymmetric (non-turbulent) transport, adequate modeling of the electron and ion heat fluxes to the divertor plates requires resolving the energy distribution function for suprathermal particles, which implies a very large total number of macroparticles per cell [9]. For instance, as pointed out in Ref. [9] for the case of a PIC code written in one dimension of configuration space, to have a moderate noise level of $\sigma \sim 1/\sqrt{N_c} \sim 0.1$ for particles with energy $\varepsilon_c T = 10T$, requires $\left[\varepsilon \exp(-\varepsilon)\sigma^2\right]^{-1} \approx 10^6$ particle per cell. Here, N_c is the number of macroparticles with energy ε_c, and T is the effective temperature of the particle distribution. These and other issues motivate the use of continuum kinetic codes for the numerical modeling of a tokamak edge.

Making use of advanced numerical methods from the fluid community, and building on the success of continuum core-region codes (e.g., GYRO [10], GENE [11], etc.) and the continuum edge code TEMPEST [8], the Edge Simulation Laboratory collaboration (ESL) [12] has started development of a new continuum kinetic code COGENT for edge plasma simulations. The code is distinguished by the use of a fourth-order finite-volume (conservative) discretization [13-14] combined with arbitrary mapped multiblock grid technology [14] (nearly field-aligned on blocks) to handle the complexity of divertor geometry with high accuracy. Another distinguishing feature of the code is the use of the Colella-Sekora flux-limiter to suppress unphysical oscillations about discontinuities while maintaining high-order accuracy elsewhere [15]. Finally, the code is written in $v_\parallel$-μ (parallel velocity – magnetic moment) variables, which avoids "cut-cell" issues appearing, for instance, when E - μ (energy – magnetic moment) variables are used such that the $v_\parallel = 0$ phase-space boundary does not align with the mesh.

It is of great importance for gyrokinetic code development to analyze numerical and physical properties of reduced collision models, as well as to achieve a detailed understanding of code performance in neoclassical simulations, which is an important step in the process of modeling the complex tokamak plasma dynamics [16-19]. In the present work we report on the implementation of a succession of increasingly comprehensive collision operators, and discuss their performance in neoclassical simulations carried out using the local closed-flux-surface

version of the COGENT code. This work extends our previous analysis [20] to including the effects of a self-consistent electric field, and also implementing more detailed collision options. In particular, here we discuss the implementation and testing of a recently proposed model linearized collision operator [21].

Finally, we present self-consistent neoclassical simulations performed for the case of steep density gradients, $L \sim \rho_{i\theta}$, characteristic of a tokamak edge under H-mode conditions. Here, $\rho_{i\theta}$ is the poloidal ion gyro-radius, and L is the radial length-scale for variation of the plasma density. Recent analytical studies demonstrated that a strong radial electric field consistent with these steep density gradients can have a significant influence on the properties of neoclassical transport in a tokamak pedestal [22-24]. In particular, a suppression of the ion heat flux, and a change in the poloidal ion flow direction in a weakly collisional (banana) regime were demonstrated. In this work we present first numerical simulations of these phenomena demonstrating qualitative agreement with the results of the analytical calculations.

The paper is organized as follows: The simulation model is summarized in Sec. II. In Sec. III we report on benchmark exercises using the simple Krook collision model to test the code performance in self-consistent neoclassical simulations. The implementation and testing of the Lorentz operator and the model linearized collision operator are discussed in Secs. IV and V, respectively. Finally, in Sec. VI, we present the results of neoclassical simulations taking into account the effects of a strong (self-consistent) radial electric field.

II. SIMULATION MODEL

The present 4D version of the COGENT code solves an axisymmetric gyrokinetic equation for a gyrocenter distribution function $f_\alpha(\mathbf{R}, v_\parallel, \mu, t)$ written in conservative form [25]

$$\frac{\partial B^*_{\parallel\alpha} f_\alpha}{\partial t} + \nabla\left(\dot{\mathbf{R}}_\alpha B^*_{\parallel\alpha} f_\alpha\right) + \frac{\partial}{\partial v_\parallel}\left(\dot{v}_\parallel B^*_{\parallel\alpha} f_\alpha\right) = B^*_{\parallel\alpha} C_\alpha[f_\alpha]. \tag{1}$$

Here, α denotes the particle species, ∇ is the gradient with respect to $\mathbf{R}$, and the guiding center velocity $\dot{\mathbf{R}}$ is given by

$$\dot{\mathbf{R}}_\alpha = \frac{1}{B^*_{\parallel\alpha}}\left[v_\parallel \mathbf{B}^*_\alpha + \frac{1}{Z_\alpha e}\mathbf{b}\times\left(Z_\alpha e\nabla\Phi + \mu\nabla B\right)\right]. \tag{2}$$

The evolution of the guiding center parallel velocity is determined from

$$\dot{v}_\parallel = -\frac{1}{m_\alpha B_{\parallel\alpha}^*} \mathbf{B}_\alpha^* \cdot (Z_\alpha e \nabla \Phi + \mu \nabla B), \tag{3}$$

where m_α and Z_α are the species mass and charge state, respectively, e is the electron charge, $\Phi(\mathbf{R},t)$ describes the long wavelength neoclassical electrostatic potential variation, $\mathbf{B}(\mathbf{R}) = B\mathbf{b}$ is the magnetic field with $\mathbf{b}$ denoting the unit vector along the field, $\mathbf{B}_\alpha^*(\mathbf{R}, v_\parallel) \equiv \mathbf{B} + (m_\alpha v_\parallel / Z_\alpha e)\nabla \times \mathbf{b}$, and $B_{\parallel\alpha}^*(\mathbf{R}, v_\parallel) \equiv \mathbf{B}_\alpha^* \cdot \mathbf{b}$. Finally, $C[f_\alpha]$ denotes the collision operator, and the presently available collision models include a simple drag-diffusion operator in parallel velocity [20], Krook collisions (Sec. III), Lorentz collisions (Sec. IV), and a linearized model Fokker-Planck collision operator conserving momentum and energy [21] (Sec. V).

The present version of the code utilizes a long wavelength approximation, $k_\perp \rho_\alpha \ll 1$, to represent the gyrokinetic Poisson equation for electrostatic potential variations in the form [25],

$$\Delta^2 \Phi = 4\pi e \left(n_e - \sum_\alpha n_{\alpha,gc} \right) - 4\pi e^2 \sum_\alpha \frac{Z_\alpha^2}{m_\alpha \Omega_\alpha^2} \nabla_\perp \cdot \left(n_{\alpha,gc} \nabla_\perp \Phi \right). \tag{4}$$

Here, $\rho_\alpha = V_{T,\alpha}/\Omega_\alpha$ is the particle thermal gyroradius, $\Omega_\alpha = Z_\alpha e B/(m_\alpha c)$ is the cyclotron frequency, $k_\perp^{-1}$ represents the characteristic length-scale for variations of the electrostatic potential, $\nabla_\perp \equiv \nabla - \mathbf{b}(\mathbf{b} \cdot \nabla)$, and the guiding center density $n_{\alpha,gc}$ is specified by

$$n_{\alpha,gc} = \frac{2\pi}{m_\alpha} \int B_{\parallel\alpha}^* dv_\parallel d\mu \left\{ f_\alpha + \frac{m_\alpha c^2}{B Z_\alpha^2 e^2} \mu \nabla_\perp^2 f_\alpha \right\}. \tag{5}$$

Electrons can be modeled either kinetically or through use of a Boltzmann (in the linear limit, adiabatic) approximation, with various options for the coefficient of the Boltzmann factor [14, 26]. In particular, for the single-ion-species neoclassical simulations reported in this work, we use a Boltzmann model for the electron density of the form

$$n_e = \langle n_{i0} \rangle \frac{\exp[e\Phi/T_e(\psi)]}{\langle \exp[e\Phi/T_e(\psi)] \rangle}, \tag{6}$$

Here, ψ is the poloidal flux function, $T_e(\psi)$ corresponds to the electron temperature distribution across magnetic flux surfaces, n_{i0} is the initial ion density distribution, and $Z_i=1$ is assumed. Making use of the long wavelength approximation, we neglect the small "pressure-term" corrections [the second term in the curly brackets in Eq. (5)] and adopt $n_{i,gc} = (2\pi/m_i)\int f_i B_{\parallel i}^* dv_\parallel d\mu$ and $n_{i0} = (2\pi/m_i)\int f_i(t=0)B_{\parallel i}^* dv_\parallel d\mu$ for the COGENT

implementation of the gyro-Poisson system. The flux surface average operator introduced in Eq. (6) is defined as

$$\langle Y \rangle (\psi) = \oint Y \frac{dl_\theta}{B_\theta} \bigg/ \oint \frac{dl_\theta}{B_\theta} , \tag{7}$$

where the integration should be taken one turn around the torus in the polodial direction. Finally, for all neoclassical simulations discussed here, the Neumann boundary condition, $\partial\Phi/\partial\psi=0$, is imposed at the domain boundaries. Note that the electron model in Eq. (6) yields a zero flux surface averaged radial electron particle flux. The quasi-neutrality of the "final" quasi-stationary state therefore requires the corresponding flux surface averaged ion particle flux to be zero as well.

The COGENT code has various options for the magnetic field geometry. In particular, the Miller model [27] is available to describe a closed flux surface (core) region. Also, X-point (single-null) geometry is available in the divertor version of the code. For simplicity, here we consider a magnetic geometry with concentric circular flux surfaces yielding

$$B_\varphi(r,\theta) = B_T R_0 / (R_0 + r\cos\theta), \tag{8a}$$

$$B_\theta(r,\theta) = B_p R_0 / (R_0 + r\cos\theta). \tag{8b}$$

Here, r is the minor radius coordinate, θ is the poloidal angle increasing in the counterclockwise direction, $\theta=0$ corresponds to the outer midplane, and the directions of the coordinate system unit vectors are given by $[\mathbf{e}_r \times \mathbf{e}_\varphi] = \mathbf{e}_\theta$. For the simulations reported, we adopt a "local" magnetic geometry, taking B_T and B_p to be constants. The safety factor q, and the inverse aspect ratio ε, which are used below, are defined as $q=\varepsilon B_\varphi/B_\theta$, and $\varepsilon=r/R_0$, where R_0 is the tokamak major radius. We also introduce $q_0=\varepsilon_0 B_T/B_p$ and $\varepsilon_0=r_0/R_0$, where $r_0=(r_{min}+r_{max})/2$ corresponds to the middle of the simulation domain, and r_{min} and r_{max} are the minor radius coordinates corresponding to the domain boundaries. Unless stated otherwise (e.g., Fig. 6), we present the result of the numerical simulations evaluated at $r=r_0$.

For simplicity, we consider the case of a single ion species with $Z_i=1$, and $m_i=2m_p$, where m_p is the proton mass. The initial distribution function is taken to be a local Maxwellian distribution,

$$F_M(r,\theta,v_\parallel,\mu) = \left(\frac{m_i}{2\pi T_{i0}(r)}\right)^{3/2} n_{0i}(r)\exp\left[-\frac{m_i v_\parallel^2}{2T_{i0}(r)} - \frac{\mu B(r,\theta)}{T_{i0}(r)}\right], \tag{9}$$

5

where the initial density and temperature profiles are specified by

$$n_{i0}(r) = n_0 \left\{ 1 - \kappa_n \Delta_n \tanh\left[(r - r_0)/\Delta_n \right] \right\}, \tag{10}$$

$$T_{i0}(r) = T_0 \left\{ 1 - \kappa_T \Delta_T \tanh\left[(r - r_0)/\Delta_T \right] \right\}. \tag{11}$$

The electron temperature in Eq. (6) is assumed to be equal to the ion temperature at the middle of the domain, i.e., $T_e(r) = T_0$. Finally, for future reference, we define the ion thermal velocity as $V_T = (2T_{i0}/m_i)^{1/2}$.

Neoclassical verification studies involve detailed analysis of the flux-surface-averaged radial particle and heat fluxes, as well as the parallel $V_\parallel$ and poloidal V_θ flow velocities. These quantities are calculated in the code as follows

$$\Gamma = \left\langle \int \frac{2\pi}{m_i} B_\parallel^* dv_\parallel d\mu \left(\dot{\mathbf{R}} \cdot \mathbf{e}_r \right) f \right\rangle, \tag{12}$$

$$Q = \left\langle \int \frac{2\pi}{m_i} B_\parallel^* dv_\parallel d\mu m_i \left(\frac{v_\parallel^2}{2} + \frac{\mu B}{m_i} + Z_i e\Phi \right) \left(\dot{\mathbf{R}} \cdot \mathbf{e}_r \right) f \right\rangle, \tag{13}$$

$$V_\parallel = \frac{1}{n} \left\langle \int \frac{2\pi}{m_i} B_\parallel^* dv_\parallel d\mu v_\parallel f \right\rangle, \tag{14}$$

$$V_\theta = \frac{1}{n} \int \frac{2\pi}{m_i} B_\parallel^* dv_\parallel d\mu \left(\dot{\mathbf{R}} \cdot \mathbf{e}_\theta \right) f - \frac{1}{Z_i e n} \left[\nabla \times \left(\mathbf{b} \int \frac{2\pi}{m_i} B_\parallel^* dv_\parallel d\mu \mu f \right) \right] \cdot \mathbf{e}_\theta, \tag{15}$$

where $n \equiv \int (2\pi/m_i) B_\parallel^* dv_\parallel d\mu f$, $\mathbf{e}_\theta$ denotes the unit vector in the poloidal direction, and the subscript i (denoting ions) has been suppressed in the notation for f_α, $\dot{\mathbf{R}}_\alpha$, and $\mathbf{B}_{\parallel\alpha}^*$. The diagnostics in Eq. (13) corresponds to the total (i.e., the sum of kinetic and potential) energy flux. However, in the final state where the ion particle flux Γ decays to zero, the energy flux in Eq. (13) becomes equal to the conductive heat flux [18, 28]. Details of the poloidal flow velocity diagnostics [Eq. (15)], which involves not only the guiding center flow (the first term), but also the curl of the magnetization (the second term) can be found in Ref. [29].

Although the flow velocity diagnostics introduced in Eqs. (14)-(15) seem intuitively appealing, it is important to discuss their accuracy in representing the actual velocity moments of the fully-kinetic (6D) distribution function. Note that the guiding center parallel velocity coordinate, $v_\parallel$, is not identical to a particle's parallel velocity. A finite difference associated with the so-called Banos drift [30] appears already in first order in δ_i, where $\delta_i \equiv (\rho_i/R_0) \ll 1$, and

therefore the flow velocity calculations are, in principal, only accurate in the zero order. However, for the case of the neoclassical simulations performed here, the solution to Eq. (1) remains close to the initial distribution [Eq. (9)], $f=F_M+O(\delta_i q \kappa_T R)F_M$, where $\delta_i q \kappa_T R \ll 1$. Therefore, the change of the flow velocities with time is accurately described by Eqs. (14)-(15) through order δ_i, and it is only the initial values that are missing δ_i-corrections. Moreover, for the case where $r_0 \kappa_T \sim 1$ (typical for a tokamak core) and $B_T \gg B_p$, variations in the flow velocities, $O(\delta_i q \kappa_T R)V_T$, associated with variations in the distribution function, are much larger than the missing corrections associated with the initial flows, $O(\delta_i)V_T$. Therefore, the flow velocity diagnostics given in Eqs. (14)-(15) is accurate in that regime. Note that variations in the ion flow become even more dominant relative to the initial missing corrections for the case of steep density gradients, characteristic of a tokamak pedestal under the H-mode conditions.

It is important to remark that the axisymmetric gyrokinetic simulation model specified by Eqs. (1)-(4) is not accurate enough to adequately describe the slow evolution of a long wavelength ($k_\perp L \sim 1$) neoclassical radial electric field [31-33] in a quasi-stationary state, where the particle fluxes across the magnetic surfaces are, to order δ_i^2, independent of the radial electric field (so-called intrinsic ambipolarity). However, here we restrict our studies to the analysis of a not-intrinsically-ambipolar [34] rapid initial relaxation of the local Maxwellian distribution [Eq. (9)] toward a quasi-stationary state (neoclassical quasi-equilibrium). The subsequent slow (transport time scale, $\nu_{ii}\delta_i^{-2}$) evolution of the quasi-stationary state including the evolution of a pressure profile, "intrinsically ambipolar" radial electric field and the toroidal angular momentum is not considered. Here, ν_{ii} denotes the ion-ion collision frequency.

The quasi-stationary state is characterized by radial force balance

$$\frac{Z_i e}{c}\left(V_\varphi B_\theta - V_\theta B_\varphi\right) - \frac{1}{n}\frac{dp_i}{dr} - Z_i e \frac{\partial \Phi}{\partial r} = 0, \tag{16}$$

where V_φ and V_θ are the toroidal and poloidal ion flow velocity, respectively, and $p_i=n_i T_i$ is the ion thermal pressure. The quasi-equilibrium neoclassical value of the poloidal flow velocity in Eq. (16) is set during the rapid relaxation (occurs on the collisional time scale) by the parallel viscous forces associated with the static magnetic field variation and is given by [35]

$$V_\theta = k\frac{c}{Z_i e B}\frac{dT_{i0}}{dr}. \tag{17}$$

Here, k is the poloidal flow coefficient, which depends on the plasma collisionality. For the case where $E_r \ll V_T B_\theta / c$, which is typical for a tokamak core, k is equal -2.1 in the Pfirsch-Schluter (highly collisional) regime, -0.5 in the plateau (moderately collisional) regime, and 1.17 in the banana (weakly collisional) regime [35]. In contrast to the poloidal flow, the flux-surface-averaged toroidal angular momentum, $P_\varphi = \langle m_i n_i R V_\varphi - R E_r B_p / (4\pi c) \rangle$ remains nearly constant during the rapid (collisional) relaxation. Therefore, the radial electric field corresponding to the relaxed quasi-stationary state is determined as a linear function of the initial toroidal angular momentum and the pressure gradient diamagnetic flows consistent with Eq. (16). It is also important to note that while the flux-surface-averaged toroidal angular momentum remains nearly constant, generation of poloidal variations in the toroidal velocity at the level of the diamagnetic flow velocity can occur on the fast (collisional) time scale along with the relaxation of the poloidal flow.

III. NEOCLASSICAL SIMULATIONS WITH THE KROOK COLLISION MODEL

The benchmark exercises carried out with the Krook collision model are used to test the performance of the COGENT code in self-consistent neoclassical simulations. In particular, for the case of a uniform temperature profile, $\kappa_T = 0$, we recover the Boltzman relation for the self-consistent distribution of potential variations. We then study generation of ion poloidal flow for the case of a nonuniform temperature distribution, and find the results of the numerical simulations in very good agreement with the predictions of an analytzcal calculation developed below for the case of the particle-conserving Krook model.

For the case of a single ion species, the following Krook model is used:

$$B_\parallel^* C_K[f] = -\nu_c B_\parallel^* \delta f + \eta_p \nu_c B \frac{F_M}{n_{i0}} \int B_\parallel^* d\mathrm{v}_\parallel d\mu \delta f + \eta_m \nu_c \mathrm{v}_\parallel F_M B \frac{m_i}{T_{i0}} \int B_\parallel^* d\mathrm{v}_\parallel d\mu \delta f \mathrm{v}_\parallel. \qquad (18)$$

Here, $\delta f = f - F_M$, ν_c is the collision frequency, and η_p and η_m take only the two values of either zero or unity to turn off (on) the corresponding particle and momentum restoring terms.

The results of the numerical simulations performed with the particle and momentum conserving version of the Krook model (i.e., $\eta_p = 1$, $\eta_m = 1$) for the case of a zero temperature gradient, $\kappa_T = 0$, are shown in Fig. 1. It is readily seen that, after the relaxation of the initial transients corresponding to the geodesic acoustic mode (GAM) excitations [36], the system reaches a quasi-stationary state in which the potential distribution is described by the Boltzmann
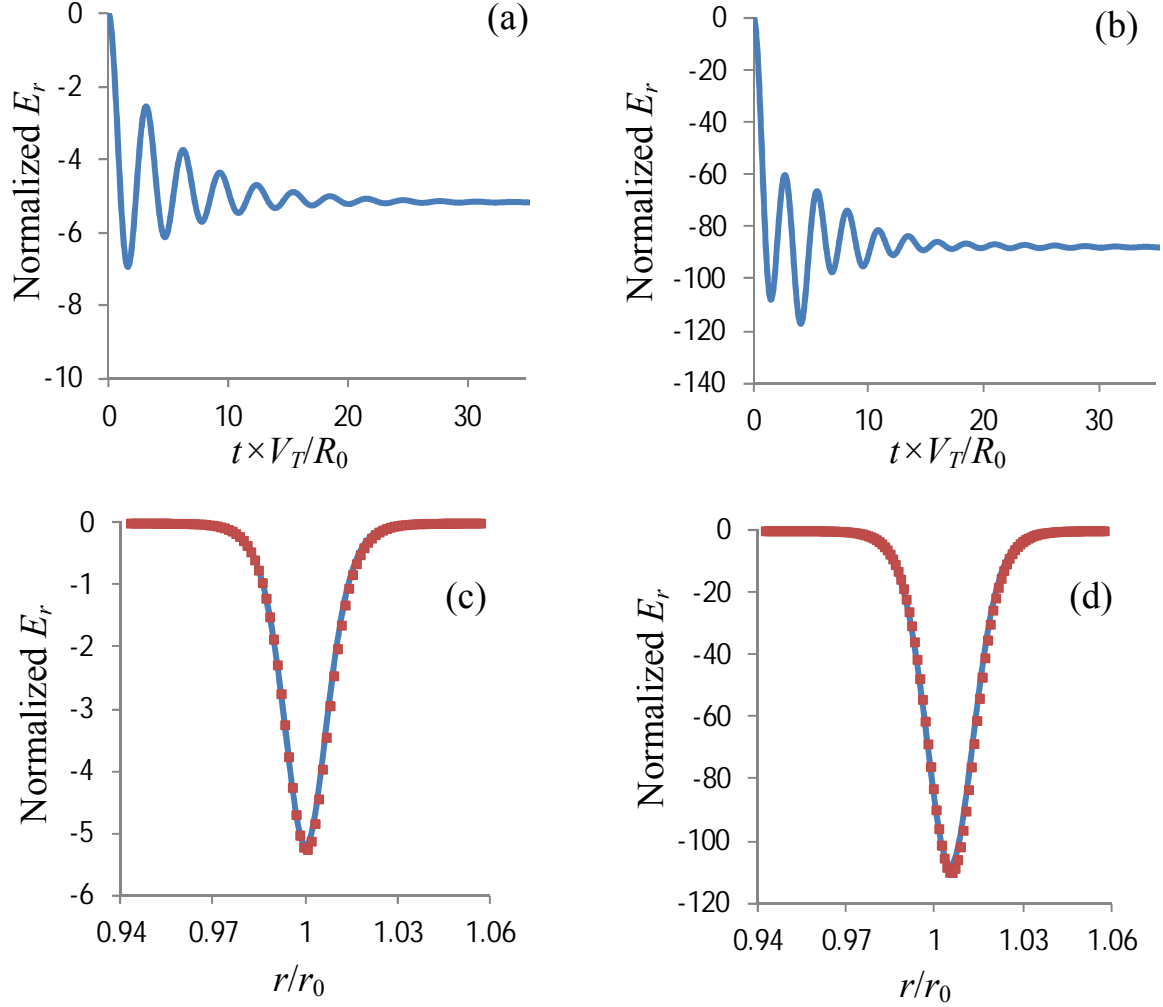
FIG 1. Neoclassical simulations for zero-temperature-gradient plasmas, $\kappa_T=0$, with small $\varepsilon^{1/2}\rho_{i\theta}\kappa_n=0.024$ [(a), (c)] and large $\varepsilon^{1/2}\rho_{i\theta}\kappa_n=0.4$ [(b), (d)] density gradients. Frames (a) and (b) show the time evolution of the normalized radial electric field, $eE_r r_0/T_0$. Frames (c) and (d) compare the radial electric field (red dots) to the Boltzmann relation (blue curve). The parameters of the simulations are $\varepsilon_0=0.1$, $q_0=1.2$, $\rho_i/R_0=1.2\times10^{-4}$, $r_0/\Delta_n=106$, $v_cV_T/qR_0=0.4$. The grid resolution is $n_r=128$, $n_\theta=16$, $n_{v\parallel}=48$, $n_\mu=32$ [(a), (c)] and $n_r=96$, $n_\theta=16$, $n_{v\parallel}=48$, $n_\mu=32$ [(b), (d)]. The velocity grid size corresponds to $|v_\parallel|_{max}/V_T=3.5$, $\mu_{max}B_\varphi/T_0=11$. Results are obtained using the particle- and momentum-conserving version of the Krook collision model, $\eta_p=\eta_m=1$.

relation, i.e. $n_i^{-1}\,dp_i/dr + e\,\partial\Phi/\partial r = 0$, consistent with negligible generation of toroidal ion flow.

Here, p_i and n_i are the ion pressure and density in the quasi-equilibrium state. The simulations also demonstrate that the Boltzmann relation remains valid even for large density gradients,

$\sqrt{\varepsilon}\rho_{i\theta}\kappa_n \sim 1$, consistent with the numerical results in Ref. [37], and analytical predictions in Refs. [38-39]. Here, $\rho_{i\theta} = V_T m_i c / (Z_i e B_p)$ denotes the poloidal gyroradius.

Next, consider the case where the temperature distribution is not uniform. The temperature gradients generate a poloidal ion flow, and the electric field is no longer described by the simple Boltzmann relation. We present an analytical calculation of the quasi-stationary radial electric field for the case of the particle conserving Krook model ($\eta_p=1$, $\eta_m=0$), assuming a large aspect ratio $\varepsilon=a/R_0 \ll 1$, and neglecting the effects of trapped particles provided $v_c \gg \varepsilon^{1/2} V_T / qR$. Note that the latter condition is different from the corresponding conventional condition $v_c \gg \varepsilon^{3/2} V_T / qR$ and is discussed in detail later in this section. Following the method developed in Ref. [40], consider a steady-state drift-kinetic equation for the first order correction to a local Maxwellian distribution, $f_1 = F - F_M$, written in energy $W = (mv^2/2 + e\Phi)$ and magnetic moment variables

$$\frac{v_\parallel}{qR}\frac{\partial f_1}{\partial \theta} + v_d \frac{\partial F_M}{\partial r}\sin\theta = -v_c f_1 + v_c \frac{F_M}{n_{i0}}\int d^3 v f_1 . \tag{19}$$

Here, the gradient of a local Maxwellian distribution, F_M [see Eq. (9)], is given by

$$\frac{\partial F_M}{\partial r}\bigg|_{W,\mu} = \left[\frac{d\ln n_{i0}}{dr} + \frac{e}{T_{i0}}\frac{\partial\Phi}{\partial r} + \left(\frac{mv^2}{2T_{i0}} - \frac{3}{2}\right)\frac{d\ln T_{i0}}{dr}\right]F_M , \tag{20}$$

$v_d = (v_\perp^2/2 + v_\parallel^2)/R\Omega_i$ is the radial drift velocity, and $v_\parallel = \sqrt{(2/m_i)[W - e\Phi(r,\theta) - \mu B(r,\theta)]}$ is a parallel velocity, which in general depends on the poloidal angle coordinate. However, under the assumptions of the present analysis, we can neglect the poloidal variations corresponding to the magnetic mirror force. Also, poloidal variations in the neoclassical electrostatic potential are generally small. Therefore, we can neglect the poloidal variations in the parallel velocity, and taking $f_1 = f_+\cos\theta + f_-\sin\theta$, it is straightforward to show that

$$\omega_t f_- + v_c f_+ - v_c \frac{F_M}{n_{i0}}\int d^3 v f_+ = 0 , \tag{21}$$

$$-\omega_t f_+ + v_c f_- - v_c \frac{F_M}{n_{i0}}\int d^3 v f_- = -v_d \frac{dF_M}{dr} , \tag{22}$$

where we introduced $\omega_t \equiv v_\parallel / qR$.

Although, it does not seem plausible to obtain an analytic solution to the system of integral equations (21)-(22), one can still calculate the flux surface average of the radial particle

10

flux, $\Gamma = \left\langle \int d^3 v f_1 v_d \sin\theta \right\rangle$, and then obtain an equation for the radial electric field from the quasi-neutrality condition, which requires zero quasi-stationary ion particle flux, $\Gamma = 0$ (see Sec. II). Note that if we were to consider a physically more adequate momentum conserving version of the Krook model (i.e., $\eta_p = \eta_m = 1$), the quasi-stationary particle flux would be *intrinsically ambipolar* (see Sec. II). That is, the quasi-stationary value of the ion particle flux would be zero through order $(\kappa_T \rho_i)^2$ (and through order $[\kappa_T \rho_i]^3$ for an up-down symmetric tokamak [33, 41]) *independent* of the radial electric field. Therefore, for the case of the momentum-conserving Krook model we would only be able to determine the combination $E_r + V_\varphi B_\theta$, but not the electric field separately (as discussed in Sec. II). Note that the fact that a quasi-stationary value of the radial electric field can be determined independently of V_φ for the case where $\eta_p = 1$, $\eta_m = 0$ is consistent with fast (collisional) relaxation of the toroidal angular momentum provided by a non-zero parallel friction force. Finally, we also note that a quasi-stationary state with zero particle flux is only consistent with a particle-conserving ($\eta_p = 1$) version of the Krook collision model. For the simplest case of a non-conservative Krook operator, i.e., $\eta_p = \eta_m = 0$, the ion particle flux would have to balance the particle production associated with the non-conservative collisional model.

It is straightforward to show from Eqs. (21)-(22) that

$$f_- - \frac{\omega_t v_c}{\omega_t^2 + v_c^2} \frac{F_M}{n_{i0}} \int d^3 v f_+ - \frac{v_c^2}{\omega_t^2 + v_c^2} \frac{F_M}{n_{i0}} \int d^3 v f_- = -\frac{v_c}{\omega_t^2 + v_c^2} v_d \frac{dF_M}{dr}, \qquad (23)$$

and it now follows that the radial particle flux that $\Gamma = (1/2) \int d^3 v f_- v_d$ is given by

$$\Gamma = -\frac{1}{2} \int d^3 v \frac{v_c}{\omega_t^2 + v_c^2} v_d^2 \frac{dF_M}{dr} + \frac{1}{2} \left(\int d^3 v f_- \right) \int d^3 v \frac{v_c^2}{\omega_t^2 + v_c^2} v_d \frac{F_M}{n_{i0}}. \qquad (24)$$

Finally, operating on Eq. (19) with $\int d^3 v$ we obtain

$$\int d^3 v f_- = -\int d^3 v \frac{v_c}{\omega_t^2 + v_c^2} v_d \frac{dF_M}{dr} \left/ \left(1 - \int d^3 v \frac{v_c^2}{\omega_t^2 + v_c^2} \frac{F_M}{n_{i0}} \right) \right. . \qquad (25)$$

The radial electric field appears in the term dF_M/dr [in Eqs. (24)-(25)] and can be found by forcing the radial particle flux in Eq. (24) to zero. For instance, when $v_c \ll V_T / qR$, corresponding to the plateau regime, we make use of $v_c / (\omega_t^2 + v_c^2) \approx \pi \delta(\omega_t)$ to obtain

$$\Gamma = -\hat{\omega}_T \rho_i^2 n_{i0} \frac{q^2 \pi^{1/2}}{4} \left(\frac{d \ln n_{i0}}{dr} + \frac{3}{2} \frac{d \ln T_{i0}}{dr} + \frac{e}{T_{i0}} \frac{d\Phi}{dr} \right), \tag{26}$$

where $\hat{\omega}_T = V_T/qR$ is the thermal transit frequency. It now follows that a quasi-stationary value of the radial electric field is given by $eE_r = n_{i0}^{-1} dp_{i0}/dr + 0.5 dT_{i0}/dr$. Neglecting the small term $eB_\theta V_\varphi/c \le 2\varepsilon T_{i0} \max\{\kappa_n, \kappa_T\} \cos\theta$ in the radial force balance equation [Eq. (16)], we readily obtain the well-known result $k = -0.5$ for the poloidal flow coefficient in the plateau regime [see Eq. (17)].

As the collision frequency decreases, the main contribution to the integrals in Eqs. (24)-(25) comes from the resonant particles whose parallel velocity satisfy $v_\parallel^{res}/qR \sim v_c$. Because the analytical model in Eqs. (19)-(20) neglects the mirror force and the effects of trapped particles, it is only valid in the regime where $v_\parallel^{res}/v \gg \varepsilon^{1/2}$, which requires $v_c \gg \varepsilon^{1/2} V_T/qR$. It is important to note that in contrast to the Krook operator in Eq. (18), a more adequate collision model (e.g., Lorentz, linearized Fokker-Planck, etc.) provides an "enhanced" collision frequency for small pitch-angle scattering, $v_{eff} \sim (v/v_\parallel)^2 v_c$. Replacing v_c with v_{eff} as done in Ref. [40] yields the conventional plateau regime condition, i.e., $v_c \gg \varepsilon^{3/2} V_T/qR$.

Finally, for the strongly-collisional (Pfirsch-Schluter) regime, the first order correction to the local Maxwellian distribution decreases with an increase in the collision frequency, $f_1 \propto v_c^{-1}$ (see Eq. [23]). Accordingly, the ion heat flux decreases as $Q \propto v_c^{-1}$, in contrast to the conventional neoclassical result predicting $Q \propto v_c^2$. This discrepancy appears due to the fact that the Krook model annihilates only a local Maxwellian distribution, implying $f_1=0$, whereas a more complete collision model has nontrivial solutions to $C[f_1]=0$.

Figure 2 shows the dependence of the poloidal velocity coefficient on the collision frequency obtained in the numerical simulations and evaluated by making use of the diagnostics defined in Eq. (15). The results of the numerical simulations are compared to the analytical predictions, where the polodial velocity coefficient is evaluated as $k = \kappa_T^{-1}(\kappa_n + \kappa_T - E_r/T_{i0})$, assuming a negligible toroidal flow velocity. This assumption, i.e., $V_\varphi B_\theta \ll V_\theta B_\varphi$, is verified for the simulations over the entire range of the collision frequencies considered. As expected from the analytical analysis, excellent agreement between the simulations and the theoretical predictions is evident for $v_c \gg \varepsilon^{1/2} V_T/qR$.
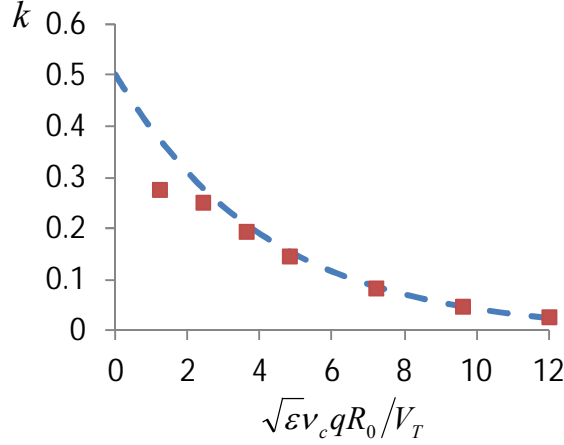
12

FIG 2. Poloidal velocity coefficient k for the case of a non-zero temperature gradient. The polodial velocity coefficient is evaluated at $\theta=\pi/2$. The parameters of the simulations correspond to $\varepsilon_0=0.01$, $q_0=1.2$, $\rho_i/R_0=4.54\times10^{-7}$, $r_0/\Delta_T=67$, $\kappa_n=0$, $\rho_{i\theta}\kappa_T=0.018$, $(r_{max}-r_{min})/r_0=0.15$. The grid resolution is $n_r=128$, $n_\theta=32$, $n_{v\parallel}=80$, $n_\mu=64$, and the velocity grid size corresponds to $|v_\parallel|_{max}/V_T=3.5$, $\mu_{max}B_\varphi/T_0=9$. Results are obtained using the particle-conserving version of the Krook collision model, i.e., $\eta_p=1$, $\eta_m=0$.

IV. LORENTZ COLLISION MODEL

We next consider the implementation of the Lorentz collision model and report on the results of neoclassical benchmark simulations. Note that the Lorentz operator is typically included in more detailed collision models, and therefore investigation of its performance is of considerable practical importance. Written using the variables of particle's speed $v=|v|$, pitch-angle $\xi=v_\parallel/v$, and gyro-angle ζ velocity, the Lorentz operator takes on a form [40]

$$C_L[f]=\frac{1}{2}\nu_D\left(\frac{v}{V_T}\right)\left[\frac{\partial}{\partial\xi}\left(1-\xi^2\right)\frac{\partial f}{\partial\xi}+\frac{1}{1-\xi^2}\frac{\partial^2 f}{\partial\zeta^2}\right]. \qquad (27)$$

Here, $\nu_D(x)=\nu_c\left[Y(x)-G(x)\right]/x^3$ is the collisional coefficient corresponding to collisions with a Maxwellian background characterized by the thermal velocity V_T, $Y(x)=\left(2/\sqrt{\pi}\right)\int_0^x e^{-y^2}dy$ is the error function, and $G(x)=\left[Y(x)-xY'(x)\right]/2x^2$. For the case of ion like-species collisions, the physical collision frequency, ν_c, corresponds to $\nu_c=4\pi n_i Z_i^4 e^4 \ln\Lambda/\left(m_i^2 V_T^3\right)$, which varies spatially owing to the ion density and temperature dependence. Here, $\ln\Lambda$ denotes the Coulomb logarithm. However, for the clarity of the verifications studies, in what follows (Secs. IV-VI), we take $\nu_c=$const with its value being specified where appropriate.

13

An accurate gyrokinetic formulation of the Lorentz operator [Eq. (27)] would involve relating particle's coordinates $(\mathbf{r}, v, \xi, \zeta)$ to the corresponding gyrokinetic variables $(\mathbf{R}, v_\parallel, \mu, \zeta_{gk})$ used in Eq. (1), and then performing proper gyroaveraging [42-43]. However, this procedure is significantly simplified for the case of long-wavelength neoclassical simulations. Note the Lorentz operator annihilates a local Maxwellian distribution function, which is also a zero order solution to the gyrokinetic Eq. (1). Therefore, in order to preserve the accuracy of the Lorentz collision model to order $\delta_i \equiv (\rho_i/R_0)$, it is sufficient to consider the lowest (zero) order relation between particle's velocity coordinates and the corresponding gyrocenter coordinates, i.e.,

$$v_\parallel \approx v_\parallel, \ v \approx \left(v_\parallel^2 + 2\mu B/m_i\right)^{1/2}, \text{ and } \zeta \approx \zeta_{gk}. \tag{28}$$

Furthermore, considering the long-wavelength (drift-kinetic) limit with $\max\{\kappa_n \rho_i, \kappa_T \rho_i\} \ll 1$, we can neglect the difference between the gyro-averaged and local quantities. Finally, we neglect the $\sim \partial^2 f/\partial \zeta^2$ term in Eq. (27), assuming that the classical gyro-diffusion is small compared to its neoclassical counterpart.

To make use of a finite-volume (conservative) numerical algorithm, we need to express the collision operator in conservative form, i.e.,

$$\overline{C}_L[f] = \frac{1}{J_{v_\parallel,\mu}} \frac{\partial}{\partial \mu}\left[J_{v_\parallel,\mu} \Pi_L^\mu(f)\right] + \frac{1}{J_{v_\parallel,\mu}} \frac{\partial}{\partial v_\parallel}\left[J_{v_\parallel,\mu} \Pi_L^{v_\parallel}(f)\right], \tag{29}$$

where $(\Pi_L^{v_\parallel}, \Pi_L^\mu)$ are the covariant coordinates of a vector flux $\mathbf{\Pi}_L$, and $J_{v_\parallel,\mu}$ is the Jacobian of the transformation $(v_x, v_y, v_z) \rightarrow (v_\parallel, \mu, \zeta_{gk})$. Consistent with Eq. (28), we consider only the lowest-order approximation, taking $J_{v_\parallel,\mu} = B/m_i$. The pitch-angle scattering part of the Lorentz operator can be represented in divergence form as

$$\frac{1}{2}\nu_D\left(\frac{v}{V_T}\right)\frac{\partial}{\partial \xi}\left(1-\xi^2\right)\frac{\partial f}{\partial \xi} = \frac{1}{J_{v,\xi}}\frac{\partial}{\partial \xi}\left[J_{v,\xi}\Pi_L^\xi(f)\right] + \frac{1}{J_{v,\xi}}\frac{\partial}{\partial v}\left[J_{v,\xi}\Pi_L^v(f)\right], \tag{30}$$

where $\Pi_L^v = 0$ and $\Pi_L^\xi = (1/2)\nu_D\left(1-\xi^2\right)\partial f/\partial \xi$ are the covariant coordinates of the vector flux $\mathbf{\Pi}_L$ in the speed-pitch angle velocity coordinate system (v, ξ, ζ), and $J_{v,\xi} = v^2$ is the Jacobian of the transformation $(v_x, v_y, v_z) \rightarrow (v, \xi, \zeta)$. Making use of the corresponding relations [44] for transformation of a vector's covariant coordinates between (v, ξ, ζ) and $(v_\parallel, \mu, \zeta_{gk})$ coordinate systems, it is straightforward to show that

$$\Pi_L^{v_\parallel}(f) = \nu_D(x)\left(\frac{\mu B}{m_i}\frac{\partial f}{\partial v_\parallel} - v_\parallel \mu \frac{\partial f}{\partial \mu}\right), \tag{31}$$

$$\Pi_L^{\mu}(f) = \nu_D(x)\left(\frac{m_i}{B}v_\parallel^2 \mu \frac{\partial f}{\partial \mu} - v_\parallel \mu \frac{\partial f}{\partial v_\parallel}\right), \tag{32}$$

where $x = \left(v_\parallel^2 + 2\mu B/m_i\right)^{1/2}/V_T$.

For the case of a single ion species, the following Lorentz model describing like-particle collisions is implemented in the code

$$B_\parallel^* C_L^{COGENT}[f] = \frac{\partial}{\partial \mu}\left[\Pi_L^{\mu}\left(B_\parallel^* \delta f\right)\right] + \frac{\partial}{\partial v_\parallel}\left[\Pi_L^{v_\parallel}\left(B_\parallel^* \delta f\right)\right] + \eta_m \nu_D v_\parallel F_M B \frac{\int B_\parallel^* dv_\parallel d\mu \delta f v_\parallel}{\int B dv_\parallel d\mu \nu_D v_\parallel F_M}, \tag{33}$$

where $\delta f = f - F_M$. The second term in Eq. (33) is a momentum restoring term, where the switch η_m takes on only zero or unity values. Note that for the sake of implementation simplicity, the collision operator in Eq. (33) contains terms $\Pi_L^{\mu}\left(B_\parallel^* \delta f\right)$ and $\Pi_L^{v_\parallel}\left(B_\parallel^* \delta f\right)$ instead of the more intuitively appealing $B_\parallel^* \Pi_L^{\mu}\left(\delta f\right)$ and $B_\parallel^* \Pi_L^{v_\parallel}\left(\delta f\right)$. However, the difference appears only in order δ_i^2, which is higher order than the gyrokinetic formulation under consideration.

Although the Lorentz operator in Eq. (33) conserves energy analytically, spurious diffusion in the energy space can appear due to the discrete (finite-difference) numerical evaluation of the pitch–angle scattering part of the operator. Note that the system's energy would be exactly conserved numerically if, for instance, energy - magnetic moment variables were used to implement the Lorentz operator. Although, the energy-magnetic moment coordinates is indeed a common choice for the implementation of a gyrokinetic system, it introduces other numerical issues, such as velocity-grid "cut-cells" at the $v_\parallel$=0 boundary. The issue of the spurious energy diffusion was addressed in more detail Ref. [20], where we demonstrated that while a 2nd order accurate implementation of the Lorentz operator generates significant numerical diffusion, a 4th order implementation suppresses it to a tolerable level. Furthermore, in the same work [20] we performed simulations of neoclassical transport making use of the Lorentz model [Eq. (33)] with η_m=0, and recovered the analytical results of Ref. [45] for the particle and heat fluxes. Note that those neoclassical simulations were performed for the case of a zero electric field and assumed $\nu_D(x)\equiv 1$.

Here we present results of neoclassical verification studies that include the effects of self-consistent electrostatic potential variations and are performed with both the conservative (η_m=1) and non-conservative (η_m=0) versions of the Lorentz model. The results of the illustrative neoclassical simulations are shown in Figs. 3 and 4. Figure 3 illustrates the time evolution of the self-consistent radial electric field corresponding to weakly-collisional (banana) and strongly-collisional (Pfirsch-Schluter) regimes. Figure 4 shows the poloidal velocity coefficient, k [see Eq. (17)], and the ion heat diffusivity,

$$\chi = -\frac{Q}{n_i \left(dT_i / dr \right)},$$ (34)

plotted for different values of the normalized collision frequency defined by [35]

$$v^* = \frac{4}{3\sqrt{\pi}} \frac{qR_0}{V_T} \varepsilon^{-3/2} v_c \frac{B_0}{B_T},$$ (35)

where $B_0 = \left(B_T^2 + B_p^2 \right)^{1/2}$. The parameters of these illustrative examples correspond to: q_0=1.2, ε_0=0.1, $\rho_{i\theta}\kappa_n$=$\rho_{i\theta}\kappa_T$=0.007, ρ_i/R_0=1.7×10^{-5}, r_0/Δ_n=r_0/Δ_T=71, and $(r_{max}$-$r_{min})/r_0$=0.1. The results of the numerical simulations are found in good agreement with the following analytical predictions.

(a) Weakly-collisional regime (v^*<<1), large aspect ratio (ε<<1), momentum-conservative Lorentz model (η_m=1).

The poloidal velocity coefficient, k, and the heat diffusivity, χ, are given in this regime approximately by [40]

$$k = 1.17 \frac{\left(1 - 1.46\sqrt{\varepsilon} \right)}{h^2},$$ (36)

$$\chi = 0.71 v_c \varepsilon^{-3/2} q^2 \frac{T_{i0}}{m_i \hat{\Omega}_i^2},$$ (37)

where $h = 1 + \varepsilon \cos\theta$, and $\hat{\Omega}_i = Z_i e B_0 / m_i c$.

(b) Weakly-collisional (banana) regime (v^*<<1), large aspect ratio (ε<<1), non-conservative Lorentz model (η_m=0).

The analysis in Ref. [40] performed for the case of a momentum-conserving Lorentz model can be generalized in a straightforward manner to obtain
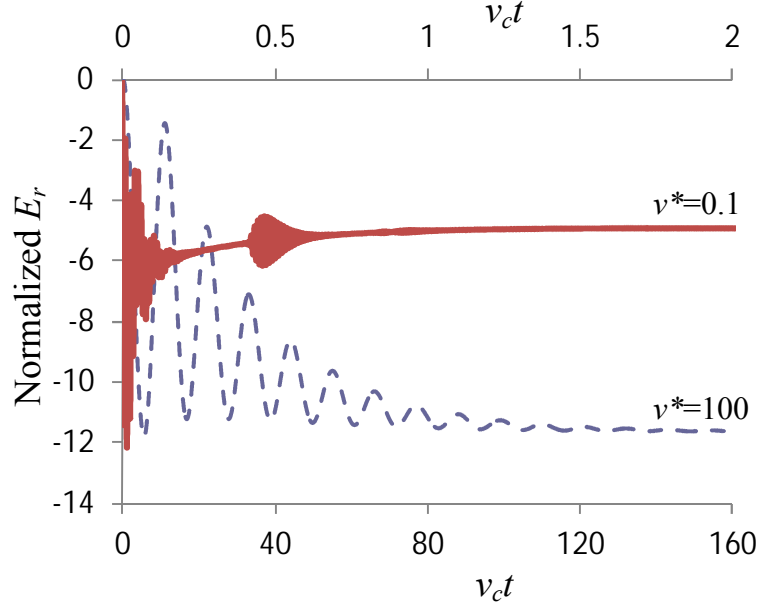
FIG 3. Time evolution of the normalized radial electric field, $eE_r r_0/T_0$, for the weakly collisional (solid red curve) and strongly collisional (dashed purple curve) cases. Results are obtained using the conservative, i.e. $\eta_m=1$, version of the Lorentz collision model. The parameters of the simulations correspond to $\varepsilon_0=0.1$, $q_0=1.2$, $\rho_i/R_0=1.7\times10^{-5}$, $r_0/\Delta_n=r_0/\Delta_T=71$, $\rho_{i\theta}\kappa_n=\rho_{i\theta}\kappa_T=0.007$, $(r_{max}-r_{min})/r_0=0.1$. The grid resolution is $n_r=32$, $n_\theta=16$, $n_{v\|}=96$, $n_\mu=48$, with $|v_\||_{max}/V_T=3$, $\mu_{max}B_\varphi/T_0=9$ in the banana regime, and $n_r=32$, $n_\theta=16$, $n_{v\|}=48$, $n_\mu=32$, with $|v_\||_{max}/V_T=3.5$, $\mu_{max}B_\varphi/T_0=11$ in the Pfirsch-Schluter regime

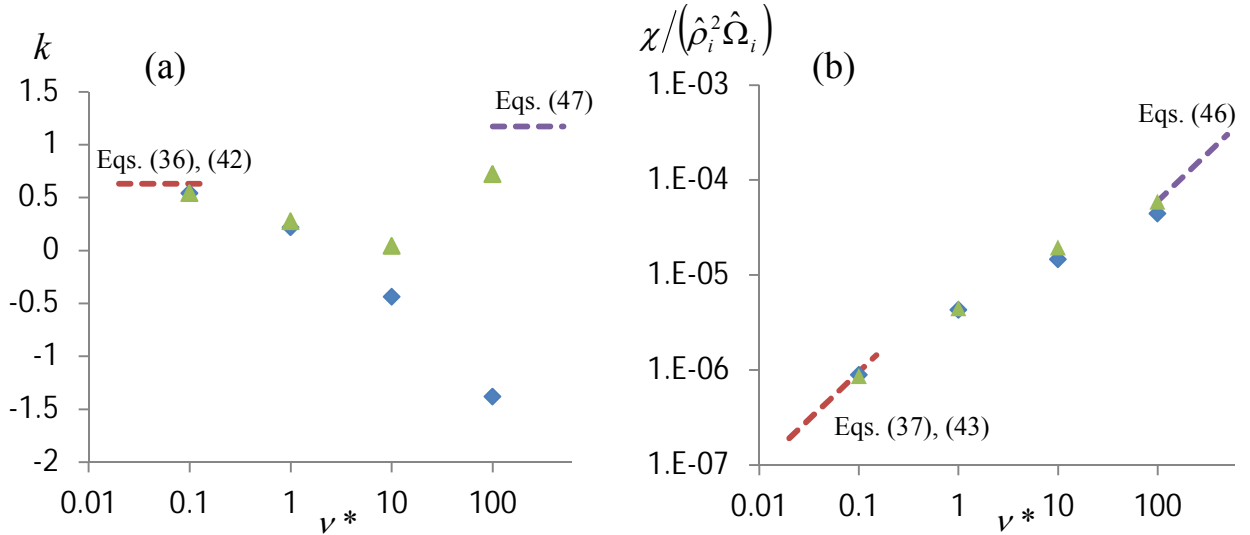

FIG 4. Plots of the poloidal velocity coefficient, k, evaluated at $\theta=\pi/2$ [frame (a)], and the normalized heat diffusivity, $\chi/(\hat\rho_i^2\hat\Omega_i)$, [frame (b)], versus the normalized collision frequency $v*$ [Eq. (35)]. Here, $\hat\rho_i = 2T_{i0}/m\hat\Omega_i^2$. The results of COGENT simulations obtained using the conservative, i.e., $\eta_m=1$, (blue diamonds) and non-conservative, i.e., $\eta_m=0$, (green triangles) versions of the Lorentz collision operator are compared against the analytical predictions given in Sec.III. The parameters of the simulations are the same as in Fig. 3.

17

$$V_\theta = \frac{\left(1 - 1.46\sqrt{\varepsilon}\right)}{h} \frac{cT}{Z_i e B_T} \left[\frac{d \ln n_{i0}}{dr} + \frac{Z_i e}{T_{i0}} \frac{d\Phi}{dr} + \left(\{x^2\} - \frac{3}{2} \right) \frac{d \ln T_{i0}}{dr} \right], \qquad (38)$$

$$Q = -\varepsilon^{-1/2} q^2 n_{i0} \frac{T_{i0}^2}{m_i \hat{\Omega}_i^2} \left[\left(\frac{d \ln n_{i0}}{dr} + \frac{Z_i e}{T_{i0}} \frac{d\Phi}{dr} - \frac{3}{2} \frac{d \ln T_{i0}}{dr} \right) \{x^2 \nu_D(x)\} + \frac{d \ln T_{i0}}{dr} \{x^4 \nu_D(x)\} \right], \qquad (39)$$

where the operator $\{A(x)\}$ is defined for an arbitrary function $A(x)$ as

$$\{A(x)\} = \frac{8}{3\sqrt{\pi}} \int_0^\infty A(x) e^{-x^2} x^4 dx. \qquad (40)$$

As discussed in Sec. III, collisions that do not conserve momentum generate a non-trivial particle flux in order $(\kappa \rho_i)^2$. Following the analysis in Ref. [40], it is straightforward to show that

$$\Gamma = -\varepsilon^{-1/2} q^2 n_{i0} \frac{T_{i0}}{m_i \hat{\Omega}_i^2} \left[\left(\frac{d \ln n_{i0}}{dr} + \frac{Z_i e}{T_{i0}} \frac{d\Phi}{dr} - \frac{3}{2} \frac{d \ln T_{i0}}{dr} \right) \{\nu_D(x)\} + \frac{d \ln T_{i0}}{dr} \{x^2 \nu_D(x)\} \right]. \qquad (41)$$

The quasi-stationary radial electric field can now be obtained from the requirement of the quasi-neutrality, which for the case of the adiabatic electron response in Eq. (6) requires $\Gamma=0$. It follows that

$$k = 1.17 \frac{\left(1 - 1.46\sqrt{\varepsilon}\right)}{h^2}, \qquad (42)$$

$$\chi = 0.71 \nu_c \varepsilon^{-3/2} q^2 \frac{T_{i0}}{m_i \hat{\Omega}_i^2}, \qquad (43)$$

which is identical to the corresponding values of the poloidal velocity coefficient and heat diffusivity obtained for the conservative version of the Lorentz collision model [Eqs. (36)-(37)]

(b) Strongly-collisional (Pfirsch-Schluter) regime ($\nu_c V_T/qR \gg 1$), large aspect ratio ($\varepsilon \ll 1$), non-conservative Lorentz model ($\eta_m = 0$).

Extending the analysis in Ref. [45] to the case where the collision frequency is an arbitrary function of a particle's speed, it is straightforward to show that

$$\Gamma = -q^2 n_{i0} \frac{2T_{i0}}{m_i \hat{\Omega}_i^2} \frac{B_0}{B_T} \left[\left(\frac{d \ln n_{i0}}{dr} + \frac{Z_i e}{T_{i0}} \frac{d\Phi}{dr} - \frac{3}{2} \frac{d \ln T_{i0}}{dr} \right) \{\nu_D(x)\} + \frac{d \ln T_{i0}}{dr} \{x^2 \nu_D(x)\} \right], \qquad (44)$$

and

$$Q = -q^2 n_{i0} \frac{2T_{i0}^2}{m_i \hat{\Omega}_i^2} \frac{B_0}{B_T} \left[\left(\frac{d \ln n_{i0}}{dr} + \frac{Z_i e}{T_{i0}} \frac{d\Phi}{dr} - \frac{3}{2} \frac{d \ln T_{i0}}{dr} \right) \{x^2 \nu_D(x)\} + \frac{d \ln T_{i0}}{dr} \{x^4 \nu_D(x)\} \right]. \qquad (45)$$

18

Again, determining the radial electric field by forcing the particle flux in Eq. (44) to zero, we obtain

$$\chi = 0.71 \nu_c q^2 \frac{2T_{i0}}{m_i \hat{\Omega}_i^2} \frac{B_0}{B_T} . \tag{46}$$

It can be shown for a strongly-collisional regime that the quasi-stationary toroidal flow velocity corresponding to the non-conservative Lorentz collision model, η_m=0, is much smaller than the diamagnetic velocity. We can therefore neglect the term $(Z_i e/c)V_\varphi B_\theta$ in Eq. (16) to obtain

$$k \cong 1.17 \frac{B_0}{B_T} . \tag{47}$$

In conclusion, we briefly discuss some features of the radial electric field time evolution. The system relaxation to a quasi-stationary state shown in Fig. 3 is accompanied by geodesic acoustic mode (GAM) oscillations [46]. There are two mechanisms for the GAM relaxation: collisional, which occurs on a collision time scale $\sim 1/\nu_c$, and collisionless phase mixing. Collisionless relaxation of long-wavelengths GAMs with $k_\perp \rho_i \ll 1$ occurs as the result of wave-particle interaction between GAMs and passing particles whose poloidal velocity satisfies the resonant condition $\left|v_\theta^{res}\right|/r \sim \omega_{GAM}$. Here, $\omega_{GAM} \sim V_T/R$ is the GAM frequency. Assuming $E_r \ll V_T B_\theta/c$, which corresponds to the parameters of the illustrative simulations in Fig. 3, it follows that $v_\theta^{res} = v_\parallel^{res} B_\theta/B$, and we obtain a well-known result $\left|v_\parallel^{res}\right| \sim q V_T$. Note that the parameters of the illustrative numerical simulations in Fig. 3 correspond to q_0=1.2, therefore the resonant velocity is close to the thermal velocity, and the collisionless relaxation is strong. In particular, it is evident for the weakly collisional regime (see Fig. 3) that the GAM relaxation occurs on a time scale less than $1/\nu_c$, i.e., the collisionless relaxation dominates. After GAM oscillations are damped, the radial electric field continues to relax to its quasi-stationary ("neoclassical") value on a collisional time scale [46].

Finally, we note that although the second burst of GAMs, which occurs at $\nu_c t \sim 0.5$ for the weakly-collisional case, can be attributed to the physical effects of nonlinear wave-particle interaction, its parameters are sensitive to the velocity grid resolution. For instance, the burst appears at a slightly later time and has a substantially smaller amplitude when the velocity-space resolution is increased. This reduction with mesh resolution implies that the burst can be also attributed to the numerical recurrence phenomena described in Ref. [47]. While a detailed

analysis of this effect is outside the scope of the present work, it is important to note that the characteristics of the system in the final relaxed (quasi-stationary) state are numerically converged. That is, an increase in the phase-space resolution does not affect the results shown in Fig 4.

V. LINEARIZED MODEL COLLISION OPERATOR

For the case where the particle distribution function is close to a local Maxwellian distribution, a linearized approximation to the full non-linear Fokker-Planck collision operator, C_{FP}, is often used to describe the like-species collisions, i.e.,

$$C_{FP}[f,f] \approx C_{FP}[\delta f, F_M] + C_{FP}[F_M, \delta f], \tag{48}$$

where $\delta f = f - F_M$. The first term on the right-hand-side of Eq. (48) describes collisions with a Maxwellian background, including energy diffusion and pitch angle scattering, and is given by [40]

$$C_{FP}[\delta f, F_M] = C_L[\delta f] + \frac{1}{2} \frac{1}{v^2} \frac{\partial}{\partial v} \left\{ v^3 \left[v_s(x) \delta f + v_{\parallel}(x) v \frac{\partial \delta f}{\partial v} \right] \right\}. \tag{49}$$

Here, $C_L[\delta f]$ is the Lorentz operator defined in Eq. (27), $x=v/V_T$ is the normalized particle speed, $v_s(x) = 4x^{-1} v_c G(x)$, and $v_{\parallel}(x) = 2x^{-3} v_c G(x)$. The constant collision frequency v_c=const and the coefficient $G(x)$ are defined in Sec. IV. The exact evaluation of the second term in Eq. (48) is, however, nearly as challenging as the evaluation of the full nonlinear Fokker-Plank operator. Therefore, in simplified linearized collision models this term is typically replaced by a few terms chosen to ensure that the model operator maintains certain features (e.g., conservation properties) of the original linearized operator [Eq. (48)]. The following linearized collision model [21] is utilized in the COGENT code

$$C_{FP}[F_M, \delta f] \rightarrow v_s \frac{2\mathbf{v} \cdot \overline{\mathbf{U}}[\delta f]}{V_T^2} F_M + v_E \frac{v^2}{V_T^2} \overline{Q}[\delta f] F_M, \tag{50}$$

where

$$v_E(v) = -\frac{v_c}{v^4 F_M} \frac{\partial}{\partial v} v^5 v_{\parallel} F_M, \tag{51}$$

and the functionals $\overline{\mathbf{U}}[\delta f]$ and $\overline{Q}[\delta f]$ are now uniquely chosen to ensure the momentum and energy conservation properties [21],

$$\overline{\mathbf{U}}[\delta f] = \frac{3}{2} \frac{\int v_s \boldsymbol{v} \delta f d^3 \boldsymbol{v}}{\int x^2 v_s F_M d^3 \boldsymbol{v}} , \qquad (52)$$

$$\overline{Q}[\delta f] = \frac{\int v^2 v_E \delta f d^3 \boldsymbol{v}}{\int v^2 x^2 v_E F_M d^3 \boldsymbol{v}} . \qquad (53)$$

As shown in Ref. [21], this model linearized collision operator [Eqs. (48)-(53)] ensures the following properties of the original linearized collision operator: it conserves particles, momentum, and energy, obeys Boltzmann's H-theorem (collisions cannot decrease entropy), and vanishes for the case where δf is represented by a linear combination of F_M, $\boldsymbol{v}F_M$, and $v^2 F_M$.

A detailed gyrokinetic formulation of the linearized model operator [Eqs. (48)-(53)] is given in Ref. [21]. However, for the case of long-wavelength neoclassical simulations considered in this work it is sufficient to use the simplified "drift-kinetic" version of the operator (see Sec. IV), which takes on the following form in the $(v_\parallel, \mu)$ coordinates

$$B_\parallel^* C_{LINEAR}^{COGENT}[f] = \frac{\partial\left(\Pi_L^\mu + \Pi_{ED}^\mu\right)}{\partial \mu} + \frac{\partial\left(\Pi_L^{v_\parallel} + \Pi_{ED}^{v_\parallel}\right)}{\partial v_\parallel} + \eta_m M_R + \eta_E \left\{ \frac{\partial \Pi_{ER}^\mu}{\partial \mu} + \frac{\partial \Pi_{ER}^{v_\parallel}}{\partial v_\parallel} \right\}. \quad (54)$$

The first two terms on the right-hand-side of Eq. (54) correspond to $C_{FP}[\delta f, F_M]$ in Eq. (48), where the collisional Lorentz fluxes $\Pi_L^{v_\parallel}$ and Π_L^μ are specified by Eqs. (31) and (32), and the energy-diffusion collision fluxes $\Pi_{ED}^{v_\parallel}$ and Π_{ED}^μ are given by

$$\Pi_{ED}^{v_\parallel} = \frac{1}{2} v_s(x) v_\parallel B_\parallel^* \delta f + \frac{1}{2} v_\parallel(x) v_\parallel \left(2\mu \frac{\partial B_\parallel^* \delta f}{\partial \mu} + v_\parallel \frac{\partial B_\parallel^* \delta f}{\partial v_\parallel} \right), \qquad (55)$$

$$\Pi_{ED}^\mu = v_s(x) \mu B_\parallel^* \delta f + v_\parallel(x) \mu \left(2\mu \frac{\partial B_\parallel^* \delta f}{\partial \mu} + v_\parallel \frac{\partial B_\parallel^* \delta f}{\partial v_\parallel} \right). \qquad (56)$$

Note that similar to the implementation of the Lorentz operator (see Sec. III), the collision fluxes in Eqs. (55)-(56) are calculated for the combination $B_\parallel^* \delta f$. From Eqs. (50) and (52) it follows that the momentum restoring term M_R is

$$M_R = v_s(x) v_\parallel F_M B \frac{\int B_\parallel^* dv_\parallel d\mu \delta f v_\parallel}{\int B dv_\parallel d\mu v_s(x) v_\parallel F_M} . \qquad (57)$$

The last two terms in the curly brackets on the right-hand-side of Eq. (54) correspond to the conservative (divergent) form of the energy restoring term, where

$$\Pi_{ER}^{v_\parallel} = -\frac{1}{2} v_s(x) v_\parallel B F_M \frac{\int B_\parallel^* dv_\parallel d\mu x^2 v_E(x)\delta f}{\int B dv_\parallel d\mu x^4 v_E(x) F_M} , \tag{58}$$

$$\Pi_{ER}^{\mu} = -v_s(x) \mu B F_M \frac{\int B_\parallel^* dv_\parallel d\mu x^2 v_E(x)\delta f}{\int B dv_\parallel d\mu x^4 v_E(x) F_M} . \tag{59}$$

Finally, as in Sec. IV, $x = \left(v_\parallel^2 + 2\mu B/m_i\right)^{1/2}\big/V_T$, $\delta f = f - F_M$, and the switches η_m and η_E take on only zero or unity values. The model energy restoring term specified by Eqs. (50)-(51) can be implemented in the conservative form [see Eqs. (54) and (58)-(59)], and therefore the finite-volume (conservative) discretization scheme provides exact (numerical) particle conservation.

The implementation of the model linearized operator [Eqs. (54)-(59)] has been tested in a series of verification studies. First, accurate annihilation of the distribution function perturbation δf represented by a linear combination of F_M, $v_\parallel F_M$, and $v^2 F_M$ is demonstrated. Next, Fig. 5 shows the results of the neoclassical simulations performed with the model linearized operator. The system parameters assumed in these simulations are the same as in Fig. 4 (see. Sec IV). The results of the numerical simulations for the poloidal velocity coefficient, k, and heat diffusivity, $\chi = -Q/[n_i(dT_i/dr)]$, are compared to approximate analytical predictions that take into account the effects of a finite inverse aspect ratio (ε) and provide interpolation between the weakly collisional (banana) and strongly collisional (Pfirsch-Schluter) regimes. Figure 5 illustrates the NCLASS-code [48] predictions for the poloidal velocity coefficient, and Chang-Hinton predictions [49] for the ion heat diffusivity. Assuming no Shafranov shift [consistent with the magnetic geometry in Eq. (8)], the Chang and Hinton approximation has the following form:

$$\chi = K_2 \varepsilon^{1/2} \frac{\rho_{i\theta}^2}{\tau_i} . \tag{60}$$

Here, $\rho_{i\theta} = V_T m_i c\big/(Z_i e B_p)$ is the poloidal gyroradius, $\tau_i = 3\sqrt{\pi}\big/(2\sqrt{2}v_c)$, and the coefficient K_2 is given by

$$K_2 = \frac{0.66 + 1.88\sqrt{\varepsilon} - 1.54\varepsilon}{1 + 1.03\sqrt{v*} + 0.31v*}\left(1 + \frac{3}{2}\varepsilon^2\right) + \frac{0.58\varepsilon v*}{1 + 0.74\varepsilon^{3/2}v*}\left(1 + \frac{3}{2}\varepsilon^2 - \sqrt{1-\varepsilon^2}\right), \tag{61}$$

where the normalized collision frequency is given in Eq. (35).

Figure 5 shows that the results of the simulations are found to be consistent with the analytical predictions in Refs. [48-49]. Note, however, that exact agreement should not be
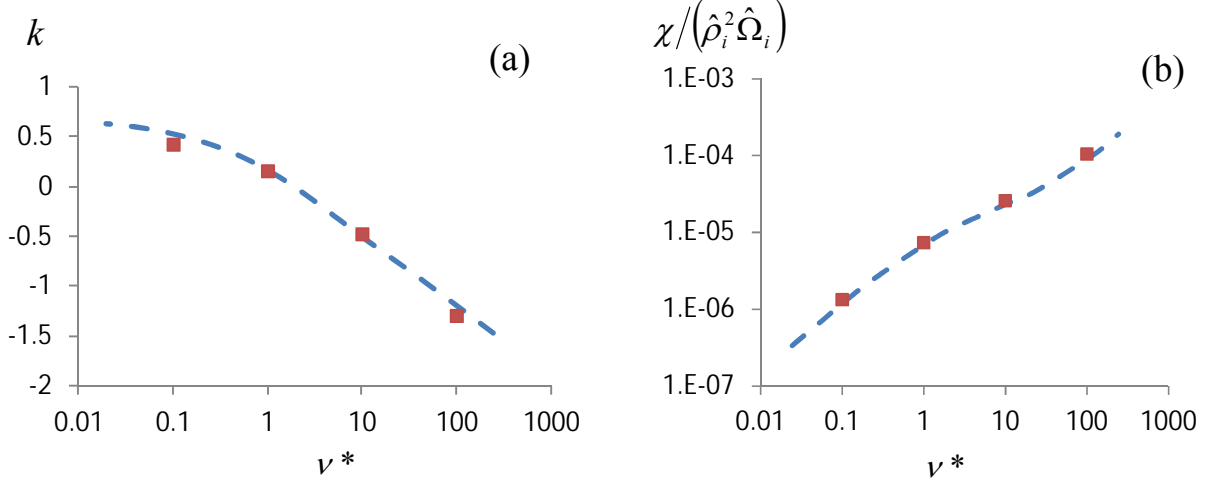
FIG 5. Plots of the poloidal velocity coefficient, k, evaluated at the outer midplane ($\theta=0$), [frame (a)], and the normalized heat diffusivity, $\chi/\left(\hat{\rho}_i^2\hat{\Omega}_i\right)$, [frame (b)], versus the normalized collision frequency v^* [Eq. (35)]. The results of the COGENT simulations (red dots) are compared with the results obtained with the NCLASS code [blue dashed curve in frame (a)], and the Chang-Hinton analytical approximation [blue dashed curve in frame (b)] given in Eqs. (60)-(61). The parameters of the simulations correspond to $\varepsilon_0=0.1$, $q_0=1.2$, $\rho_i/R_0=1.7\times10^{-5}$, $r_0/\Delta_n=r_0/\Delta_T=71$, $\rho_{i\theta}\kappa_n=\rho_{i\theta}\kappa_T=0.007$, $(r_{max}-r_{min})/r_0=0.1$. The grid resolution is $n_r=32$, $n_\theta=16$, $n_{v\parallel}=96$, $n_\mu=48$, with $|v_\parallel|_{max}/V_T=3$, $\mu_{max}B_\varphi/T_0=9$ in the banana regime, and $n_r=32$, $n_\theta=16$, $n_{v\parallel}=48$, $n_\mu=32$, with $|v_\parallel|_{max}/V_T=3.5$, $\mu_{max}B_\varphi/T_0=11$ in the Pfirsch-Schluter regime. Results are obtained using the momentum and energy conserving form, i.e., $\eta_E=\eta_m=1$, of the model linearized operator given in Eq. (54).

expected since the analytical studies assume collision models that are different from the one given in Eqs. (54)-(59), and furthermore there are no analytical methods for a rigorous treatment of the intermediate collisionality regime, i.e., $v^*\sim1$. The level of quantitative discrepancy is found to be similar to that observed in verification studies performed with other gyrokinetic codes [17-18].

V. EFFECTS OF A STRONG RADIAL ELECTRIC FIELD

The properties of neoclassical transport can be significantly affected by a strong radial electric field corresponding to

$$E_r \sim V_T B_\theta/c. \tag{62}$$

A radial electric field of this magnitude can be present in the steep edge of a tokamak under H-mode conditions. Indeed, the length scale for plasma density variations in a tokamak edge can be of the order of the poloidal ion gyroradius, $\kappa_n\rho_{i\theta}\sim1$, and the estimate in Eq. (62) follows from the radial force balance equation [Eq. (16)], provided the ion flow velocities are less than the thermal velocity, i.e., V_θ, $V_\varphi < V_T$.

Recent analytical studies demonstrated that the presence of the strong radial electric field given in Eq. (62) significantly modifies the conventional results of the neoclassical formalism developed for a tokamak core region where $E_r \ll V_T B_\theta / c$ [22-23]. In particular, it was shown that a strong radial electric field provides suppression of the neoclassical ion heat flux. Also, it was demonstrated for a weakly collisional (banana) regime that the poloidal ion flow can change its direction as compared with its core counterpart. The modifications come primarily from the fact that the conventional neoclassical analysis neglects the $E \times B$ drift velocity contribution to the poloidal advection term in the ion drift-kinetic equation, i.e., $\left(\dot{\mathbf{R}} \cdot \mathbf{e_\theta} \right) r^{-1} \partial f / \partial \theta \approx \left(v_\parallel / qR \right) \partial f / \partial \theta$ is assumed. While this assumption is typically valid in the tokamak core region, the presence of a strong radial electric field in the edge [Eq. (62)] makes the contribution of the $E \times B$ drift to the ion poloidal velocity comparable to the parallel streaming contribution, and therefore it can no longer be neglected [22-23]. Retaining the $E \times B$ piece of the advection velocity in the analysis of the quasi-stationary neoclassical equilibrium, i.e., $\left(\dot{\mathbf{R}} \cdot \mathbf{e_\theta} \right) r^{-1} \partial f / \partial \theta \approx \left(v_\parallel / qR + c E_r B_\varphi / B^2 r \right) \partial f / \partial \theta$, has important consequences. In particular, the $E \times B$ velocity modifies the shape of the boundary between trapped and passing particles, shifting it toward the tail of the ion distribution function. For a weakly collisonal regime, this leads to a suppression of ion heat flux and a change in the poloidal flow direction [22].

The gyrokinetic model implemented in the COGENT code [Eqs. (1)-(4)] offers an accurate description of long-wavelength neoclassical physics including the parameter regime where a radial electric field is the order that in Eq. (62), provided $B_\theta \ll B_\varphi$. It is therefore of considerable practical interest to numerically investigate the effects of a strong radial electric field on the neoclassical transport coefficients. Figure 6 shows the results of the numerical simulations corresponding to the case of a weakly collisional regime with $\nu^* = 0.3$ obtained using the conservative version of the linearized collision model, i.e., $\eta_m = \eta_E = 1$. Each data set illustrated in Fig. 6, which includes the poloidal velocity coefficient, ion heat diffusivity and normalized radial electric field, corresponds to an independent simulation distinguished by its value of the initial density gradient, κ_n. All data sets are evaluated at the radial coordinate $r \approx 0.98 r_0$, corresponding to a local maximum value of the radial electric field for the simulation with the steepest density gradient. In order reduce the computational time required to simulate slow (nearly-collisionless) relaxation of large-amplitude GAM oscillations associated with steep density gradients, we start the simulations (in Fig. 6) with a higher collision frequency, $\nu^* = 10.5$.
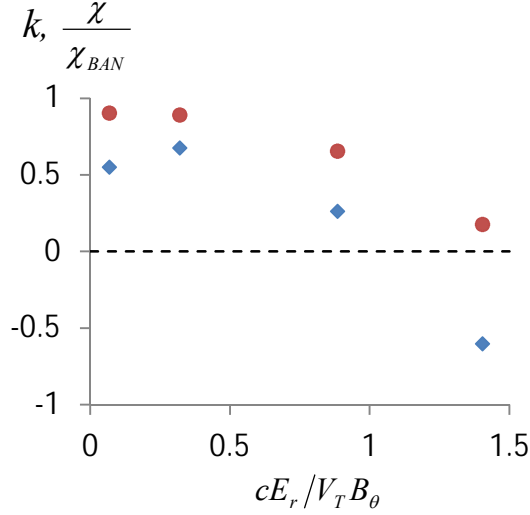
24

FIG 6. Plots of the poloidal velocity coefficient, k (blue diamonds), and the normalized ion heat diffusivity, χ/χ_{BAN} (red circles) evaluated at $\theta=\pi$ and $r\approx0.98r_0$, versus the normalized radial electric field. Here, χ_{BAN} is the weakly-collisional ion heat diffusivity given in Eq. (37). The parameters of the simulations are $\varepsilon_0=0.029$, $q_0=1.2$, $\nu^*=0.3$, $\rho_i/R_0=9.2\times10^{-5}$, $r_0/\Delta_n=r_0/\Delta_T=21$, $\rho_{i\theta}\kappa_T=-0.13$, $(r_{max}-r_{min})/r_0=0.4375$, $|v_{\|}|_{max}/V_T=3.5$, $\mu_{max}B_\phi/T_0=9$. The normalized density gradients used in the simulations correspond to $-\rho_{i\theta}\kappa_n=0.13; 0.67; 1.61; 2.2$. The grid resolution is [$n_r=48$, $n_\theta=32$, $n_{v\|}=96$, $n_\mu=48$], and [$n_r=64$, $n_\theta=32$, $n_{v\|}=128$, $n_\mu=80$] for the simulations with the minimum and maximum values of the density gradient, respectively. Results are obtained using the momentum and energy conservative form, i.e., $\eta_E=\eta_m=1$, of the model linearized operator given in Eq. (54).

As the GAMs are rapidly (collisionally) damped, the collision frequency is slowly (adiabatically) reduced to its steady-state value of $\nu^*=0.3$. Finally, we consider inverse density and temperature profiles, i.e., $\kappa_n<0$, $\kappa_T<0$, for the simulations presented in this section. While similar results are obtained in the interior of the simulation domain for either sign of κ_n and κ_T, fewer numerical artifacts near the domain boundaries are observed for the case where $\kappa_n<0$, $\kappa_T<0$.

Consistent with the analytical prediction in Ref. [22], the simulations recover a change in the poloidal velocity direction and a suppression of ion heat flux. However, there is also a pronounced quantitative discrepancy. The latter can plausibly be attributed to finite inverse aspect ratio (ε) corrections. Indeed, the analytical analysis in Ref. [22] retains only the lowest order effects in ε. For instance, in the limit of a small radial electric field $E_r\ll V_TB_\theta/c$, corresponding to the conventional neoclassical formalism, the analysis in Ref. [22] recovers $k=1.17$. However, for the case of $\varepsilon_0=0.029$, which is used in the present illustrative simulations, a more accurate estimate [Eq. (36)] predicts a significantly different value, $k=0.88$. Also, the differences between the linearized collision model in Eqs. (54)-(59) and that used in Ref. [22]

25

become increasingly important for finite values of ε. Finally, for the case of steep density gradients, $\kappa_n \rho_{i\theta} \sim 1$, and a non-uniform temperature distribution, nonlocal effects appear for finite values of ε. That is, the variations in the ion density become pronounced on the banana-width length scale, $\Delta_{ban} \sim \varepsilon^{1/2} \rho_{i\theta}$. The analytical treatment in Ref. [22] assumes the local-theory limit ($\kappa_n \Delta_{ban} \ll 1$), which implies $\varepsilon^{1/2} \ll 1$. However, this constraint is not well-satisfied in the present simulations corresponding to $\varepsilon^{1/2} = 0.17$. Also note that the collisionality constraint for a weakly collisional (banana) regime, i.e., $v^* \ll 1$, is not well-satisfied in the present simulations performed for $v^* = 0.3$. In principle, an attempt to reproduce the results of the analytical results quantitatively could be made by decreasing the collision frequency along with the inverse aspect ratio, ε. However, a significant decrease in the inverse aspect ratio below its present value of $\varepsilon_0 = 0.029$ would require simulation times beyond the scope of this initial study.

In conclusion we note that a strongly-sheared equilibrium electric field can significantly suppress turbulent transport [50], therefore a detailed analysis of neoclassical transport in the steep edge region of a tokamak is of considerable practical importance. In addition to a strong radial electric field, the edge of a diverted tokamak is distinguished by ion orbit losses, which can also significantly influence the properties of neoclassical transport. While the orbit loss effects provide a significant challenge for a detailed analytical analysis, our newly available divertor version of the COGENT code, which includes both the pedestal and the scrape-off-layer (SOL) regions, will allow us to perform a detailed numerical investigation of these phenomena.

IV. CONCLUSIONS

In this paper we report on the development and application of the nonlinear continuum gyrokinetic code COGENT for edge plasma simulations. The code is distinguished by the use of a fourth-order finite-volume (conservative) discretization combined with arbitrary mapped multiblock grid technology (nearly field-aligned on blocks) to handle the complexity of divertor geometry with high accuracy. While the discussion of the numerical algorithms and the initial advection tests is reported elsewhere [13-14], the present work discusses the implementation of various collision models and analyzes code results for advanced neoclassical simulations including the effects of self-consistent variations in the electrostatic potential. In particular, we discuss the implementation and testing of the Krook, Lorentz and recently proposed model

linearized collision operators [21]. The results of the neoclassical simulations performed with these operators are found to be in good agreement with various analytical predictions.

In addition, we give results of the first numerical simulations of neoclassical transport including the effects of a strong (self-consistent) radial electric field on the ion poloidal flow and heat flux. Recent analytical studies [22-23] demonstrated that the presence of a strong radial electric field of order $E_r \sim V_T B_p / c$, which is consistent with a subsonic pedestal equilibrium under H-mode conditions, modifies the conventional results of the neoclassical formalism developed for the core region, where $E_r << V_T B_p / c$. In particular, it was shown that a strong radial electric field provides suppression of the neoclassical ion heat flux. In addition, it was demonstrated for a weakly collisional (banana) regime that the poloidal ion flow can change its direction as compared with its core counterpart. These earlier findings were applied to elucidate the discrepancy between the conventional banana regime predictions and recent experimental measurements of the impurity flow performed on the Alcator C-Mod tokamak [24]. The results of the self-consistent numerical simulations obtained using the COGENT code in a weakly collisional regime are found to be in good qualitative agreement with the theoretical predictions in Ref. [22]. In particular, a change in the poloidal ion flow direction and a suppression of the ion heat flux are demonstrated. A quantitative discrepancy between the results of the analytical analysis and the numerical simulations is discussed and shown likely due to a combination of finite aspect-ratio, finite orbit-size, and finite-collision-frequency effects. Finally, we note again that the results of the self-consistent neoclassical simulations for the case of steep density gradients (characteristic of a tokamak edge) are obtained with the closed-flux-surface version of the code. Our future work will extend the analysis to include the effects of ion orbit losses by making use of the newly available divertor version of the COGENT code, which includes both the pedestal and the scrape-off-layer regions.

REFERENCES

[1] R. H. Cohen and X. Q. Xu, Contrib. Plasma Phys. **48**, 212 (2008), and references therein.

[2] C. S. Chang, and S. Ku, Phys. Plasmas **15**, 062510 (2008).

[3] J. A. Heikkinen, T. P. Kiviniemi, T. Kurki-Suonio, A.. Peeter, S. K. Sipilia, J. Comp. Phys. **173**, 527 (2001)

[4] J. A. Heikkinen, S. Henriksson, S. Janhuhen, T.P. Kiviniemi and F. Ogando, Contr. Plasma Phys. **46**, 490 (2006).

[5] T. Takizuka, M. Hosokawa and K. Shimizu, Trans. Fusion Tech. **39**, 111 (2001).

[6] Y. Idomura, M. Ida, S. Tokuda, Commun. Nonlinear Sci. Numer. Simul.**13**, 227 (2007).

[7] B Scott, Plasma Phys. Control. Fusion **48** A387 (2006).

[8] X. Q. Xu, Z. Xiong, M. R. Dorr, J. A. Hittinger, K. Bodi, J. Candy, B. I. Cohen, R. H. Cohen, P. Colella, G.D. Kerbel, S. Krasheninnikov, W. M. Nevins, H. Qin, T. D. Rognlien, P. B. Snyder and M. V. Umansky, Nucl. Fusion **47,** 809 (2007)

[9] O. V. Batishchev, S. I. Krasheninnikov, Peter J. Catto, A. A. Batishcheva, D. J. Sigmar, X. Q. Xu, J. A. Byers, T. D. Rognlien, R. H. Cohen, M. M. Shoucri, and I. P. Shkarofskii, Phys. Plasmas **4**, 1672 (1997).

[10] J. Candy and R. E. Waltz, Phys. Rev. Lett. **91** (2003) 045001.

[11] T. Görler, X. Lapillonne, S. Brunner, T. Dannert, F. Jenko, F. Merz, and D. Told, Journal of Computational Physics **230**, 7053 (2011).

[12] Edge Simulation Laboratory (https://esl.lbl.gov)

[13] P. Colella, M. R. Dorr, J. A. F. Hittinger, and D. F. Martin, J. Comput. Phys. **230**, 2952 (2011).

[14] M. R. Dorr, R. H. Cohen, P. Colella, M. A. Dorf, J. A. F. Hittinger, and D. F. Martin, *Proceedings of the SciDAC 2010 Conference*, Tennessee (2010).

[15] P. Colella and M. D. Sekora, J. Computat. Phys. **227** 7069 (2008).

[16] E. A. Belli and J. Candy, Plasma Phys. Control. Fusion **50**, 095010 (2008).

[17] G. Dif-Pradalier, P. H. Diamond, V. Grandgirard, Y. Sarazin, J. Abiteboul, X. Garbet, Ph. Ghendrih, G. Latu, A. Strugarek, S. Ku, and C. S. Chang, Phys. Plasmas **18**, 062309 (2011).

[18] T. Vernay, S. Brunner, L. Villard, B. F. McMillan, S. Jolliet, T. M. Tran, A. Bottino, and J. P. Graves, Phys. Plasmas **17**, 122301 (2010).

[19] X. Q. Xu, Phys. Rev. E **78** 016406 (2008).

[20] M. A. Dorf, R. H. Cohen, J. Compton, M. Dorr, J. Compton, T. Rognlien, J. Angus, S. Krasheninnikov, P. Colella, D. Martin, and P. McCorquodale, Contr. Plasma Phys. **52**, 518 (2012).

[21] I. G. Abel, M. Barnes, S. C. Cowley,W. Dorland, and A. A. Schekochihin, Phys. Plasmas **15**, 122509 (2008).

[22] G. Kagan and P. Catto, Plasma Phys. Control. Fusion, **52**, 055004 (2010).

[23] I. Pusztai and P. Catto, Plasma Phys. Control. Fusion, **52**, 075016 (2010).

[24] G. Kagan, K. D. Marr, P. J. Catto, M. Landerman, B. Lipschultz, R. McDermott. Plasma Phys. Control. Fusion, **53**, 025008 (2011).

[25] T. S. Hahm, Phys. Plasmas **3**, 4658 (1996).

[26] R. H. Cohen, M. Dorf, and M. Dorr, Contrib. Plasma Phys. **52**, 529 (2012).

[27] R. L. Miller, M. S. Chu, J. M. Greene, Y. R. Lin-Liu, and R. E. Waltz, Phys. Plasmas **5**, 973 (1998).

[28] P. Helander, Plasma Phys. Control. Fusion **37**, 57 (1995).

[29] R. D. Hazeltine and J. D. Meiss, *Plasma Confinement* (Addison-Wesley, Redwood City, 1992).

[30] A. Banos, J. Plasma Phys. **1**, 305 (1967).

[31] F. I. Parra and P. J. Catto, Plasma Phys. Control. Fusion **50**, 065014 (2008).

[32] F. I. Parra and P. J. Catto, Phys. Plasmas **17**, 056106 (2010).

[33] A. N. Simakov, X. Z. Tang, and R. Kolesnikov, *2010 International Sherwood Fusion Theory Conference*, Seattle, Washington, 2010.

[34] S. P. Hirshman, Nucl. Fusion **18**, 917 (1978).

[35] F. Hinton and R. Hazeltine, Rev. Mod. Phys. **48**, 239 (1976).

[36] N. Winsor, J. L. Johnson, and J. M. Dawson, Phys. Fluids **11**, 2448 (1968).

[37] W. X. Wang, F. L. Hinton, and S. K. Wong, Phys. Rev. Lett. **87**, 055002 (2001).

[38] G. Kagan and P. J. Catto, Plasma Phys. Control. Fusion **50**, 085010 (2008).

[39] P. J. Catto and R. Hazeltine, Phys. Plasmas **13**, 122508 (2006).

[40] P. Helander and D.J. Sigmar, *Collisional Transport in Magnetized Plasmas* (Cambridge University Press, Cambridge, 2002).

[41] S. K. Wong and V. S. Chan, Phys. Plasmas **12**, 092513 (2005).

[42] A. J. Brizard, Phys. Plasmas **11**, 4429 (2004).

[43] Chang Liu, Hong Qin, Chenhao Ma, and Xiongjie Yu, Phys. Plasmas **18**, 032502 (2011).

[44] G. A. Korn and T. M. Korn, *Mathematical Handbook for Scientists and Engineers*, (Mcgraw-Hill, 1967).

[45] Z. Lin, W. M. Tang, and W. W. Lee, Phys. Plasmas **2**, 2975 (1995).

[46] S. V. Novakovskii, C. S. Liu, and R. Z. Sagdeev, and M. N. Rosenbluth, Phys. Plasmas **4**, 4272 (1997).

[47] M. J. Pueschel, T. Dannert, and F. Jenko, Comput. Phys. Commun. **181**, 1428 (2010).

[48] W. A. Houlberg, K.C. Shaing, S.P. Hirshman, M.C. Zarnstorff, Phys. Plasmas **4**, 3230 (1997).

[49] C. S. Chang and F. L. Hinton, Phys. Fluids **25**, 1493 (1982).

[50] K. H. Burrell, Phys. Plasmas **4**, 1499 (1997).